

Numerical Simulation of the Behavior for a Vortex Ring Convecting along the Axis of a Rotating Field

Tomomi Uchiyama^{1*}, Masato Nakano² and Tomohiro Degawa³

¹EcoTopia Science Institute, Nagoya University, Furo-cho, Chikusa-ku, Nagoya 464-8603, Japan

²JFE KANKYO Corporation, 3-1 Benten-cho, Tsurumi-ku, Yokohama 230-0044, Japan

³Numazu National College of Technology, 3600, Ooka, Numazu, Shizuoka 410-8501, Japan

Abstract

This study simulates the behavior of a vortex ring on a field rotating with a constant angular velocity. The vortex ring convects along the rotating axis of the field. The Reynolds number based on the circulation of the vortex ring is 500, and the rotation number defined with the circulation and the angular velocity ranges from 0 to 0.4. The simulation highlights secondary vortex rings at the head and in the rear of the vortex ring, a streamwise longitudinal vortex around the central (rotating) axis, and a swirling flow along the vortex core. The generation of such vortical structures by the Coriolis force is explored. The simulation also discusses the effect of the rotation number on the time-evolution characteristics of the vortex ring.

Keywords: Vortex ring; Rotating field; Vortex method; Coriolis force; Helicity

Introduction

In relation with the knowledge of air currents in the atmosphere and the grasp of the flow in turbomachinery, the flows on rotating fields have been attracting a number of researchers. The experimental and numerical studies have been conducted mainly for incompressible flows. The effect of the Coriolis force on the flow stability [1], the change in the turbulence structures due to the field rotation [2,3], the characteristics of the secondary flows [4,5], and the hydrodynamic losses [5,6] have been made clear.

Vortices are among the most important and fundamental composites of flow structures. The comprehension of the dynamics promises to contribute the clarification of various turbulent phenomena. Vortex ring has attracted much attention on account of the simple geometry [7], and some researches of the behavior on rotating fields have been reported. Eisenga et al. [8] conducted an experimental study using a rotating water tank. A vortex ring was launched in the direction perpendicular to the rotating axis, and the deformation and the change in the convection motion were explored. Verzicco et al. [9] carried out an experimental investigation on a vortex ring launched in the direction parallel to the rotating axis. They investigated a secondary vortex ring, the vorticity of which is of opposite sign to that of the vortex ring, appearing at the head of the vortex ring. They also reported the occurrence of a swirling flow around the central axis behind the vortex ring. Brend and Thomas [10] confirmed such swirling flow behind the vortex ring by an experiment similar to that of Verzicco et al. For a vortex ring convecting along the rotating axis, however, the velocity and vorticity induced by the Coriolis force as well as the time-evolution characteristics have not been fully studied.

This study simulates the behavior of a vortex ring convecting along the axis of a rotating field to clarify the effect of the Coriolis force on the velocity and vorticity fields. Vortex in cell (VIC) method is employed for the simulation. It is one of the vortex methods for incompressible flows. It discretizes the vorticity field into vortex elements and computes the time evolution of the flow by tracing the convection of each vortex element using the Lagrangian approach. The Lagrangian calculation markedly reduces the numerical diffusion and also improves numerical stability. Thus, the VIC method is eminently suitable for direct numerical simulation (DNS) of turbulent flows [11-

13]. One of the authors [14] has previously proposed the improvements of the VIC method, and demonstrated the validity by applying the improved VIC method to the DNS of a turbulent channel flow. This study uses the improved VIC method. The simulation confirms that the strength of the vortex ring decreases as the angular velocity of the flow field increases and that secondary vortex rings appear at the head and in the rear of the vortex ring. The simulation also makes clear that a streamwise longitudinal vortex appears around the central (rotating) axis behind the vortex ring and that a swirling flow occurs along the vortex core.

Basic Equations and Simulation Method

Conservation equations for flow

Let us consider an incompressible flow on a field rotating with a constant angular velocity. The mass and momentum conservation equations written in a reference frame rotating with the field are given by

$$\nabla \cdot \mathbf{u} = 0 \quad (1)$$

$$\frac{\partial \mathbf{u}}{\partial t} + (\mathbf{u} \cdot \nabla) \mathbf{u} = -\frac{1}{\rho} \nabla p + \nu \nabla^2 \mathbf{u} - 2\boldsymbol{\Omega} \times \mathbf{u} \quad (2)$$

where $\boldsymbol{\Omega}$ is the angular velocity, and p is the modified pressure which includes the centrifugal effect.

Taking the curl of Eq. (2) and substituting Eq. (1) into the resultant equation, the vorticity equation is derived. The vorticity equation, expressed in the non-dimensional form by using the diameter D_0 and circulation Γ_0 of a vortex ring at the initial time, is written as

***Corresponding author:** Tomomi Uchiyama, EcoTopia Science Institute, Nagoya University, Furo-cho, Chikusa-ku, Nagoya 464-8603, Japan, E-mail: uchiuyama@is.nagoya-u.ac.jp

Received November 29, 2013; **Accepted** January 14, 2015; **Published** January 22, 2015

Citation: Uchiyama T, Nakano M, Degawa T (2015) Numerical Simulation of the Behavior for a Vortex Ring Convecting along the Axis of a Rotating Field. J Vortex Sci Technol 2: 107. doi: [10.4172/2090-8369.1000107](https://doi.org/10.4172/2090-8369.1000107)

Copyright: © 2015 Uchiyama T, et al. This is an open-access article distributed under the terms of the Creative Commons Attribution License, which permits unrestricted use, distribution, and reproduction in any medium, provided the original author and source are credited.

$$\frac{\partial \boldsymbol{\omega}}{\partial t} + \nabla \cdot (\boldsymbol{\omega} \mathbf{u}) = \nabla \cdot (\mathbf{u} \boldsymbol{\omega}) + \frac{1}{\text{Re}} \nabla^2 \boldsymbol{\omega} + \text{Ro} (\mathbf{k} \cdot \nabla) \mathbf{u} \quad (3)$$

where $\boldsymbol{\omega} (= \nabla \times \mathbf{u})$ is the vorticity, and \mathbf{k} is the unit vector parallel to the rotating axis. The Reynolds number Re and the rotation number Ro are defined as

$$\text{Re} = \Gamma_0 / \nu \quad (4)$$

$$\text{Ro} = 2\Omega D_0^2 / \Gamma_0 \quad (5)$$

Orthogonal decomposition of velocity

According to the Helmholtz theorem, the velocity \mathbf{u} is the sum of the gradient of a scalar potential ϕ and the curl of a vector potential $\boldsymbol{\Psi}$:

$$\mathbf{u} = \nabla \phi + \nabla \times \boldsymbol{\Psi} \quad (6)$$

The velocity calculated by (6) remains unaltered when any gradient of a scalar potential function is added to $\boldsymbol{\Psi}$. To remove this arbitrariness, the following solenoidal condition is imposed on $\boldsymbol{\Psi}$:

$$\nabla \cdot \boldsymbol{\Psi} = 0 \quad (7)$$

Taking the curl of Eq. (6) and substituting Eq. (7) into the resultant equation, we obtain the following vector Poisson equation for $\boldsymbol{\Psi}$:

$$\nabla^2 \boldsymbol{\Psi} = -\boldsymbol{\omega} \quad (8)$$

Similarly, substituting Eq. (6) into Eq. (1) and recognizing that $\nabla \cdot (\nabla \times \boldsymbol{\Psi}) = 0$, we obtain the Laplace equation for ϕ :

$$\nabla^2 \phi = 0 \quad (9)$$

Discretization of vorticity field into vortex elements

Once $\boldsymbol{\Psi}$ and ϕ have been computed from Eqs. (8) and (9) respectively, the velocity \mathbf{u} is calculated from Eq. (6). The vorticity $\boldsymbol{\omega}$ in Eq. (8) is estimated from Eq. (3). The VIC method discretizes the vorticity field into vortex elements, and calculates the distribution of $\boldsymbol{\omega}$ by tracing the convection of each vortex element.

It is postulated that the position and vorticity for the vortex element p are $\mathbf{x}_p = (x_p, y_p, z_p)$ and $\boldsymbol{\omega}_p$, respectively. The Lagrangian form of the vorticity equation, Eq. (3), is written as follows:

$$\frac{d\mathbf{x}_p}{dt} = \mathbf{u}(\mathbf{x}_p) \quad (10)$$

$$\frac{d\boldsymbol{\omega}_p}{dt} = \nabla \cdot (\mathbf{u}(\mathbf{x}_p) \boldsymbol{\omega}(\mathbf{x}_p)) + \frac{1}{\text{Re}} \nabla^2 \boldsymbol{\omega}(\mathbf{x}_p) + \text{Ro} (\mathbf{k} \cdot \nabla) \mathbf{u}(\mathbf{x}_p) \quad (11)$$

When the position and vorticity of a vortex element are known at time t , the values at $t = t + \Delta t$ are computed from Eqs. (10) and (11). In the VIC method, the flow field is divided into computational grid cells to define $\boldsymbol{\Psi}$, ϕ and $\boldsymbol{\omega}$ on the grids. If $\boldsymbol{\omega}$ is defined at a position $\mathbf{x}_k = (x_k, y_k, z_k)$, the vorticity $\boldsymbol{\omega}$ is assigned to \mathbf{x}_k , or a vortex element with $\boldsymbol{\omega}$ is redistributed onto \mathbf{x}_k .

$$\boldsymbol{\omega}(\mathbf{x}_k) = \sum_p^{N_p} \boldsymbol{\omega}_p W \left(\frac{x_k - x_p}{\Delta x} \right) W \left(\frac{y_k - y_p}{\Delta y} \right) W \left(\frac{z_k - z_p}{\Delta z} \right) \quad (12)$$

where N_p is the number of vortex elements, and Δx , Δy and Δz are the grid widths. For the redistribution function W , the following equation is employed [15].

$$W(\varepsilon) = \begin{cases} 1 - 2.5\varepsilon^2 + 1.5|\varepsilon|^3 & |\varepsilon| < 1 \\ 0.5(2 - |\varepsilon|)^2(1 - |\varepsilon|) & 1 \leq |\varepsilon| \leq 2 \\ 0 & |\varepsilon| > 2 \end{cases} \quad (13)$$

Equation (13) was used for the simulations of time-developing free shear flows [11-13]. The DNS of a turbulent channel flow [14] and that of a jet issuing from a rectangular nozzle [16] were successfully performed with Eq. (13).

Discretization with staggered grid and correction of vorticity

When solving Eqs. (8) and (9), staggered grids are used to ensure consistency between the discretized equations, and to prevent numerical oscillations of the solution [14]. Figure 1 shows the staggered grid. The scalar potential ϕ is defined at the center of the grid. The velocity \mathbf{u} is defined at the sides, while the vorticity $\boldsymbol{\omega}$ and the vector potential $\boldsymbol{\Psi}$ are defined on the edges.

In the VIC method, the vorticity field is discretized into vortex elements, and the field is expressed by superimposing the vorticity distributions around each vortex element. The superposition is performed by Eq. (12). The resulting vorticity field $\boldsymbol{\omega}_r$ does not necessarily satisfy the solenoidal condition. The authors' previous study [14] demonstrated that the curl of the velocity calculated from $\boldsymbol{\omega}_r$ yields a vorticity that satisfies the solenoidal condition. This correction method for the vorticity is employed in this simulation [15].

Numerical procedure

Given the flow at time t , the flow at $t + \Delta t$ is simulated by the following procedure:

Calculate the time variation of $\boldsymbol{\omega}_p$ at every grid point from Eq. (11).

Calculate the convection of each vortex element from Eq. (10).

Calculate $\boldsymbol{\omega}$ from Eq. (12).

Calculate $\boldsymbol{\Psi}$ from Eq. (8).

Calculate ϕ from Eq. (9).

Calculate \mathbf{u} from Eq. (6).

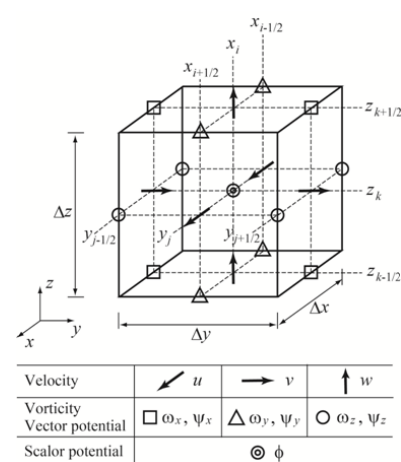
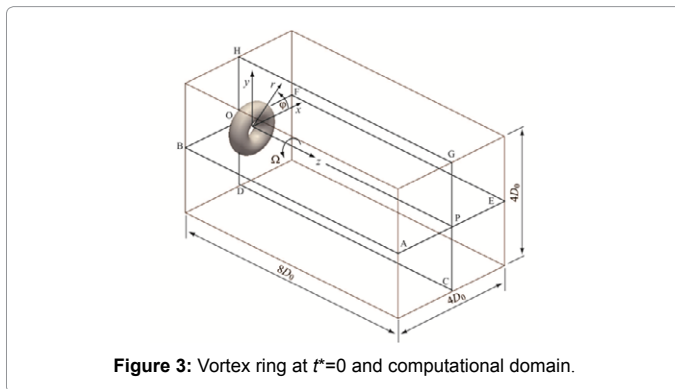
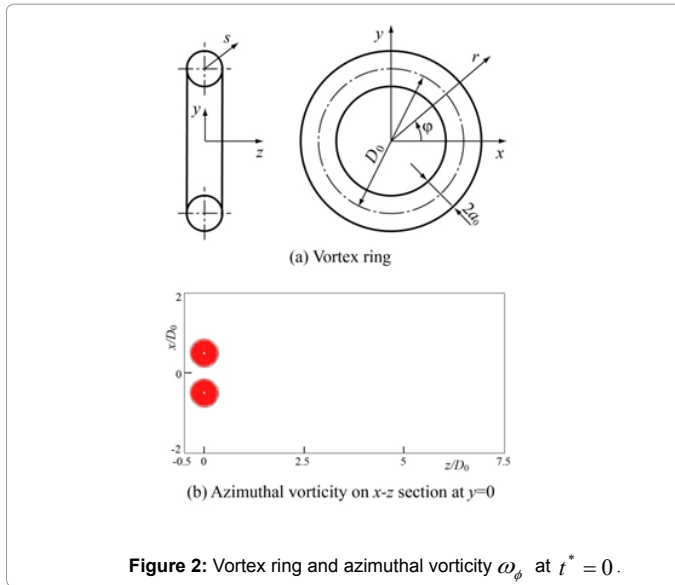


Figure 1: Staggered.



Correct the vorticity, or calculate the corrected vorticity from the curl of \mathbf{u} .

Computational Conditions

At the initial time ($t^* = 0$), the vortex ring is expressed by giving the vorticity component ω_ϕ normal to the cross-section of the vortex core. This study gives the vorticity distribution employed in the simulations of a vortex ring on a non-rotating field by Stanway et al. [17] and Wee-Ghoniem [18]. The azimuthal vorticity ω_ϕ is as follows

$$\omega_\phi = \frac{K \Gamma_0}{\pi a_0^2} \exp \left[-K \left(\frac{s}{a_0} \right)^2 \right] \quad (14)$$

where Γ_0 is the circulation and $K=2.24182^2/4$. a_0 and S are the core radius and the distance from the center of the vortex core respectively as shown in Figure 2a.

The origin of coordinates is set at the center of the vortex ring. The z -axis is parallel to the convection direction of the vortex ring. The angle between the radius vector \mathbf{r} and the x -axis is denoted by ϕ . The contours of ω_ϕ on the x - z section at $y=0$ are shown in Figure 2b.

Figure 3 shows the vortex ring at $t^* = 0$, where the iso-surface of the azimuthal vorticity ω_ϕ , $\omega_\phi / (\Gamma_0 / D_0^2) = 0.8$, is presented. The computational domain of $4D_0 \times 4D_0 \times 8D_0$ is also shown in Figure

3. The boundary behind the vortex ring locates at $z / D_0 = -0.5$. The number of grids is $80 \times 80 \times 160$. The computational domain rotates with a constant angular velocity Ω around the central axis (z -axis) of the vortex ring.

The computational conditions are listed in Table 1. The cases for the rotation number Ro of $0 \leq Ro \leq 0.2$ are simulated at the core diameter of $2a_0 / D_0 = 0.35$ and the Reynolds number of $\Gamma_0 / \nu = 500$. As the vortex ring convects in quiescent fluid, ϕ is set at zero in the computational domain, and the solution of Eq. (9) can be omitted. A slip condition is imposed on the boundaries. For example, the conditions at $x / D_0 = \pm 2$ are expressed as:

$$\frac{\partial \psi_x}{\partial x} = 0, \psi_y = 0, \psi_z = 0 \quad (15)$$

Four planes passing through the central axis of the vortex ring are set as shown in Figure 3. The strength of the vortex ring or the circulation Γ is calculated on the planes by the following equation

$$\Gamma = \frac{1}{4} \left(\int_{OPAB} \boldsymbol{\omega} \cdot \mathbf{n} dS + \int_{OPCD} \boldsymbol{\omega} \cdot \mathbf{n} dS + \int_{OPEF} \boldsymbol{\omega} \cdot \mathbf{n} dS + \int_{OPGH} \boldsymbol{\omega} \cdot \mathbf{n} dS \right) \quad (16)$$

where \mathbf{n} is the unit vector normal to the plane.

Since the abovementioned four planes include the cross-section of the vortex core, the locations, at which the velocity falls to zero, exist on each plane. This simulation regards the locations as the center of the vortex core. The coordinates of the location on each plane are averaged to detect the diameter D and z -coordinate z_v of the vortex ring.

Results and Discussion

Behavior of vortex ring on non-rotating field ($Ro=0$)

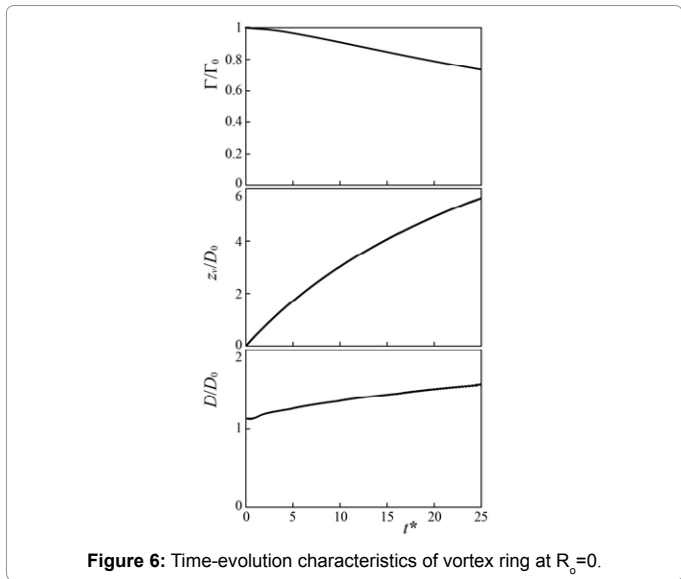
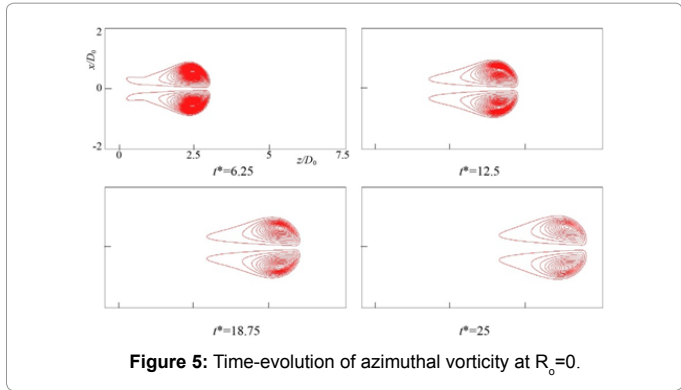
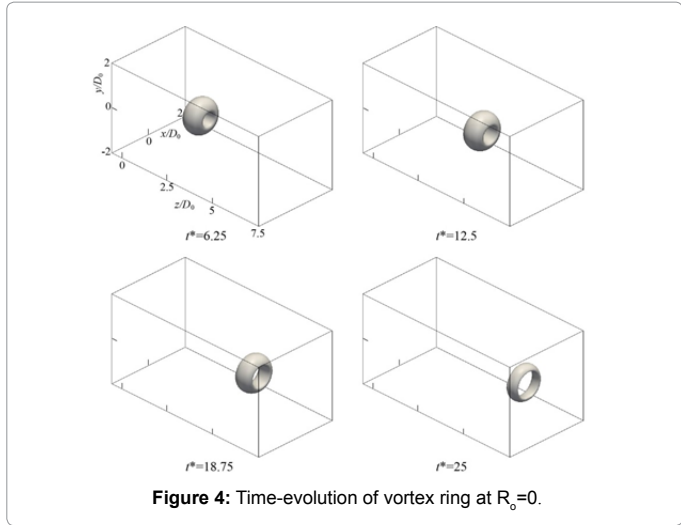
The behavior of the vortex ring on the non-rotating field ($Ro=0$) is shown in Figure 4. The azimuthal vorticity ω_ϕ representing the vortex ring is presented with the iso-surface ($\omega_\phi / (\Gamma_0 / D_0^2) = 0.8$) at four time points. The vortex ring convects along the central axis (z -axis) with maintaining its axisymmetric vorticity distribution. The strength reduces with the passage of time owing to the viscous effect.

Figure 5 shows the time evolution of ω_ϕ on the x - z cross-section at $y=0$. The vortex core is circular at $t^* = 0$ as found from Figure 2b. But it is stretched along the central axis (z -axis) at $t^* = 6.25$, becoming ellipsoidal. In the rear end of the vortex core, the contours are axially elongated. The vorticity decreases with the passage of time at $t^* \geq 6.25$. Such vorticity distribution coincides with the simulation by Wee and Ghoniem [18] at the same condition as this study. One can confirm the validity of the present simulation method.

The time-evolution characteristics of the vortex ring are shown in Figure 6. The circulation Γ / Γ_0 decreases as the time passes. This is attributable to the viscous effect, and the decrement remains unaltered

Core diameter; $2a_0 / D_0$	0.35
Reynolds number; $Re = \Gamma_0 / \nu$	500
Rotation number; $Ro = 2\Omega_0 / \Gamma_0$	0, 0.08, 0.16, 0.2
Computational domain	$4D_0 \times 4D_0 \times 8D_0$
Number of grids	$80 \times 80 \times 160$
Time increment; $\Delta t / (D_0^2 / \Gamma_0)$	0.0125

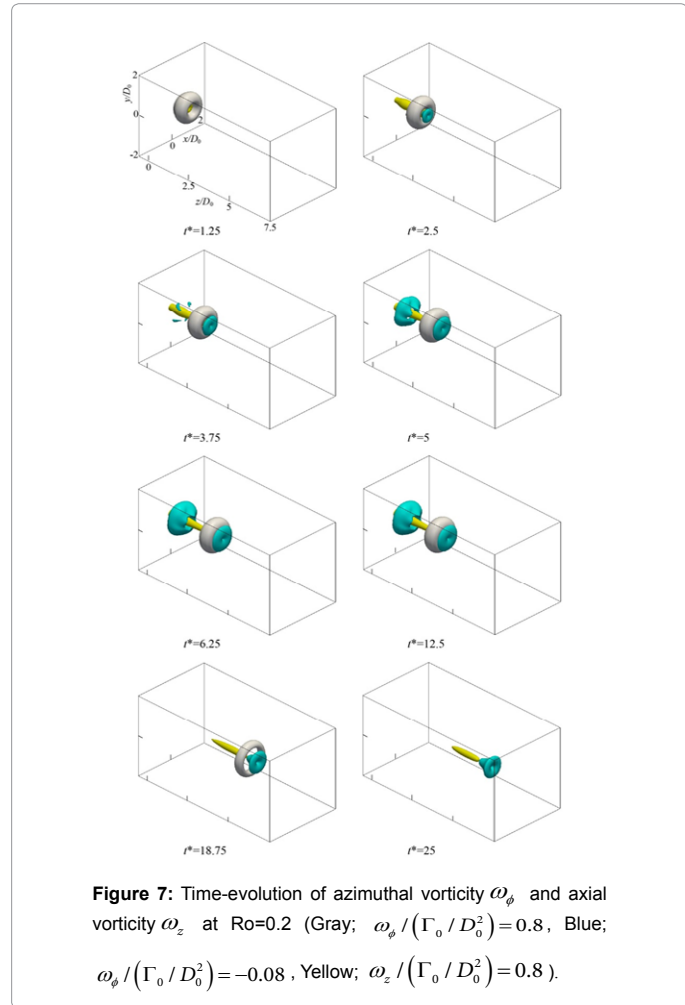
Table 1: Computational conditions.



at $t^* \geq 2.5$. The convection velocity also lowers with the passage of time because of the reduction of the circulation, as found from the time variation of the convection distance z_v / D_0 . The diameter D / D_0 increases as the time passes.

Behavior of vortex ring on rotating field ($R_o=0.2$)

The behavior of the vortex ring at the rotation number $R_o=0.2$ is shown in Figure 7, where the azimuthal vorticity ω_ϕ that presents the vortex ring is plotted by the iso-surface ($\omega_\phi / (\Gamma_0 / D_0^2) = 0.8$) in gray. The vortex ring convects straight along the rotating axis (z -axis) with maintaining its axisymmetric vorticity distribution. When compared with the result on the non-rotating field ($R_o=0$) shown in Figure 4, ω_ϕ decreases markedly with the passage of time at $t^* \geq 12.5$. The iso-surface disappears at $t^* = 25$. These are caused by a secondary vortex ring, the azimuthal vorticity of which is of opposite sign to that of the vortex ring, and accordingly it interacts with the vortex ring as mentioned later. In Figure 7, the vorticity component in the axial (z) direction, ω_z , is superimposed by the iso-surface ($\omega_z / (\Gamma_0 / D_0^2) = 0.8$) in yellow. Though the axial vorticity ω_z does not appear in the non-rotating condition ($R_o=0$), it occurs locally around the central axis near the vortex ring at $t^* = 6.25$ in the case of $R_o=0.2$. Similar vorticity field was also numerically simulated by Verzicco et al. [9] at $Re=1476$ and $R_o=0.4$. The azimuthal vorticity ω_z is composed of the azimuthal velocity U_ϕ induced by the Coriolis force as discussed later. The streamwise longitudinal vortex, represented by ω_z , is axisymmetric, and it is elongated in the axial (z) direction with the convection of the vortex ring. The strength of ω_z decreases as the passage of time at $t^* \geq 12.5$. The vorticity region of $\omega_\phi > 0$ corresponds to the vortex ring. The region of $\omega_\phi < 0$ also occurs due to the rotation



of the flow field. The iso-surface of $\omega_\phi / (\Gamma_0 / D_0^2) = -0.08$ is shown in blue. Such secondary vortex ring appears around the central axis at the head of the vortex ring when $t^* = 2.5$, and similar vortex ring also occurs in the rear of the vortex ring at $t^* = 3.75$. These secondary vortex rings are axisymmetric. In the study of Verzicco et al. [9] at $Re=738$ and $R_0=0.4$, the secondary vortex ring at the head of the vortex ring was simulated. When $t^* \geq 12.5$, the absolute value of the vorticity for the vortex ring decreases markedly with the passage of time. However, the streamwise longitudinal vortex and the secondary vortex rings, which are induced by the field rotation, less attenuate, and their iso-surfaces exist even at $t^* = 25$.

The time evolution of the distribution for the azimuthal velocity u_ϕ on the x - z section at $y=0$ is shown in Figure 8. The contours for $u_\phi / (\Gamma_0 / D_0)$ are plotted, where the contours of $u_\phi > 0$ and $u_\phi < 0$ are plotted in red and blue respectively. The region of $u_\phi > 0$ indicates that the flow direction coincides with the rotating direction of the field. The center of the vortex core is also indicated by the symbol +. The flow with $u_\phi > 0$ appears around the central axis and behind the vortex ring. The velocity constitutes the axial vorticity ω_z shown in Figure 7. The flows with $u_\phi < 0$ are observed outside of the vortex cores and at the head of the vortex ring. The absolute value of the velocity is smaller.

The appearance of the azimuthal velocity u_ϕ shown in Figure 8 is caused by the Coriolis force. In the non-rotating condition ($R_0=0$) at $t^* = 2.5$, the velocity distributes on the x - z section at $y=0$ as shown in Figure 9a. The planes at $x < 0$ and $x > 0$ are denoted by A and B, respectively. If the angle between the velocity \mathbf{u} and the rotating axis (z -axis) is denoted by θ as shown in Figure 9b and c the flow with $u_\phi > 0$ is induced by the Coriolis force on the planes A and B in the case of $0 < \theta < \pi$. Such condition for θ is satisfied by the flow toward the central (rotating) axis. It is confirmed that the condition is satisfied in the region of $u_\phi > 0$ shown in Figure 8. It should be noted that flow toward the central axis occurs behind the vortex cores, and the

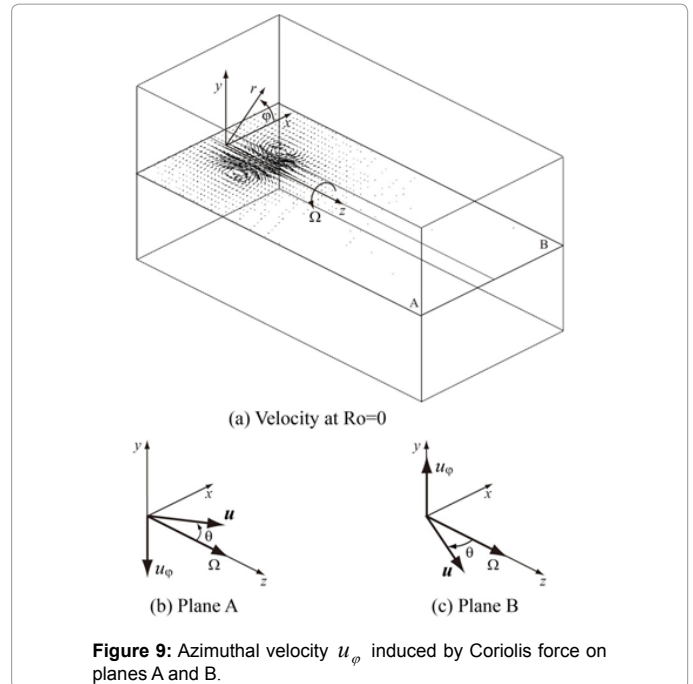


Figure 9: Azimuthal velocity u_ϕ induced by Coriolis force on planes A and B.

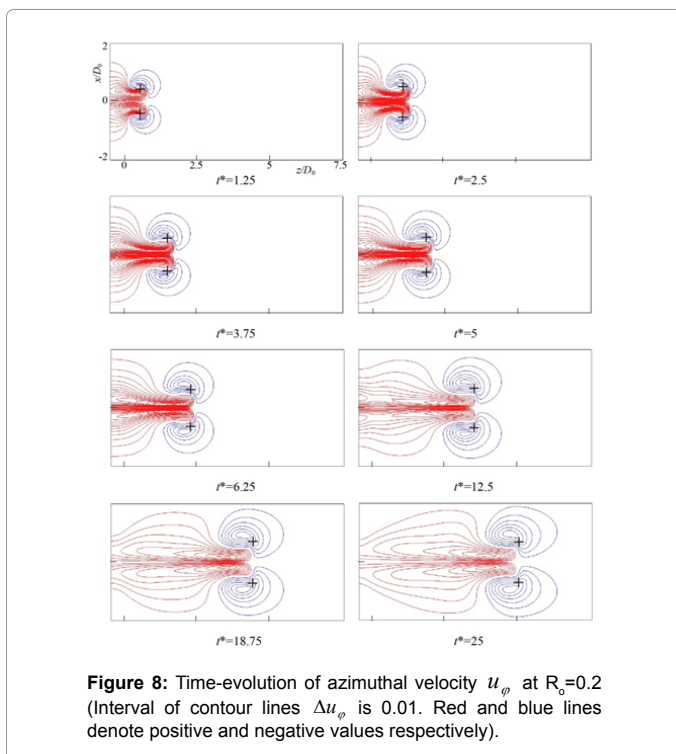


Figure 8: Time-evolution of azimuthal velocity u_ϕ at $R_0=0.2$ (Interval of contour lines Δu_ϕ is 0.01. Red and blue lines denote positive and negative values respectively).

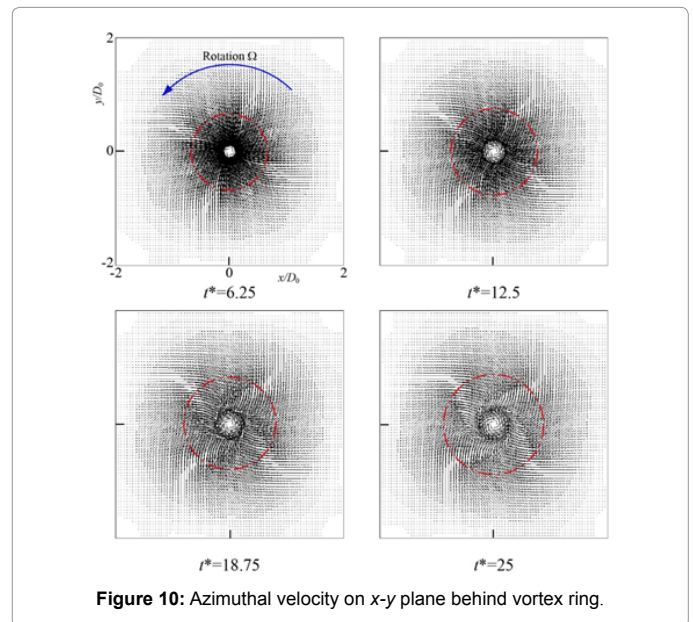


Figure 10: Azimuthal velocity on x - y plane behind vortex ring.

flow with $u_\phi < 0$ exists there as found in Figure 8. This is caused by the fact that the flow with $u_\phi < 0$ induced at the head of the vortex ring is transported to the rear part due to the vortex motion of the vortex ring.

Figure 10 shows the velocity distribution on the x - y section perpendicular to the convection direction of the vortex ring. The results on the section $0.4D_0$ behind the vortex core are depicted. A circle passing through the vortex cores is superimposed. The diameter D corresponds to the diameter of the vortex ring. The flow with $u_\phi > 0$ toward the rotating direction of the flow field is observed around the central axis, and the small-scale flow with $u_\phi < 0$ toward the opposite direction is found outside of the vortex cores.

The secondary vortex rings having the negative azimuthal vorticity

ω_ϕ are induced due to the rotation of the flow field as shown in Figure 7. The generation mechanism can be explained with the use of the vorticity equation for ω_ϕ :

$$\frac{\partial \omega_\phi}{\partial t} + \nabla \cdot (\mathbf{u}\omega)_\phi = \nabla \cdot (\mathbf{u}\omega)_\phi + \frac{1}{\text{Re}} (\nabla^2 \omega)_\phi + \text{Ro} \frac{\partial u_\phi}{\partial z} \quad (17)$$

One can find from Eq. (17) that the azimuthal vorticity ω_ϕ is induced in the region where the azimuthal velocity u_ϕ varies in the convection direction of the vortex ring (z -direction). The velocity u_ϕ decreases markedly in the z -direction around the central axis at the head of the vortex ring as discovered in Figure 8. Figure 11 shows the distribution of ω_ϕ on the x - z section at $y=0$, where the contours of $\omega_\phi < 0$ are plotted in blue. Around the central axis at the head of the vortex ring or in the abovementioned region of $\partial u_\phi / \partial z < 0$, the region of $\omega_\phi < 0$ or the secondary vortex ring is found. According to Figure 8, the region of $\partial u_\phi / \partial z < 0$ also exists in the rear of the vortex ring. In this region, the secondary vortex ring with $\omega_\phi < 0$ also appears at $5 \leq t^* \leq 12.5$ shown in Figure 11. As the absolute value of the velocity gradient $|\partial u_\phi / \partial z|$ is smaller than that at the head of the vortex ring, the strength of the secondary vortex ring is lower.

Effect of Ro on behavior of vortex ring

The iso-surfaces of the vorticity components ω_ϕ and ω_z at $\text{Ro}=0.08$ and 0.16 are shown in Figure 12, where the results at $t^*=12.5$ and 25 are plotted. When compared with the results at $\text{Ro}=0.2$ shown in Figure 7, the reduction of the strength for the vortex ring becomes larger as Ro increases. The scale of the streamwise longitudinal vortex around the central axis and that of the secondary vortex rings become larger with the increase of Ro .

Figure 13 shows the distribution of the axial velocity u_z on the

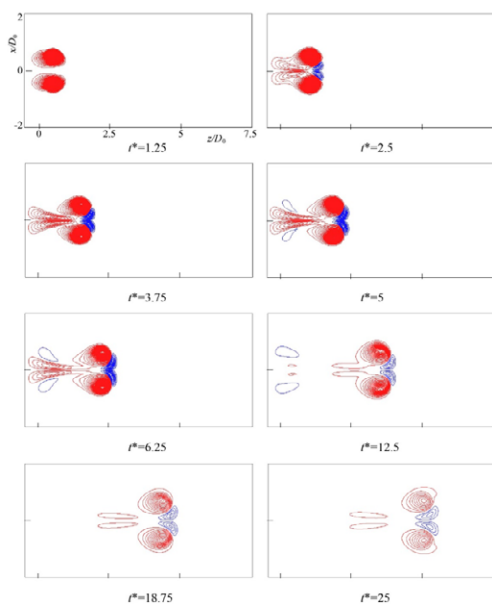


Figure 11: Time-evolution of azimuthal vorticity ω_ϕ on x - z plane at $\text{Ro}=0.2$ (Interval of contour lines $\Delta\omega_\phi$ is 0.08 . Red and blue lines denote positive and negative values respectively).

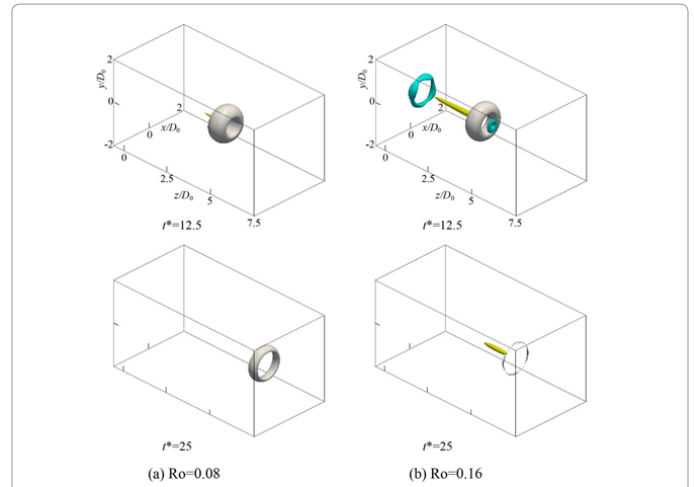


Figure 12: Azimuthal vorticity ω_ϕ and axial vorticity ω_z at $\text{Ro}=0.08$ and 0.16 (Gray; $\omega_\phi / (\Gamma_0 / D_0^2) = 0.8$, Blue; $\omega_\phi / (\Gamma_0 / D_0^2) = -0.08$, Yellow; $\omega_z / (\Gamma_0 / D_0^2) = 0.8$).

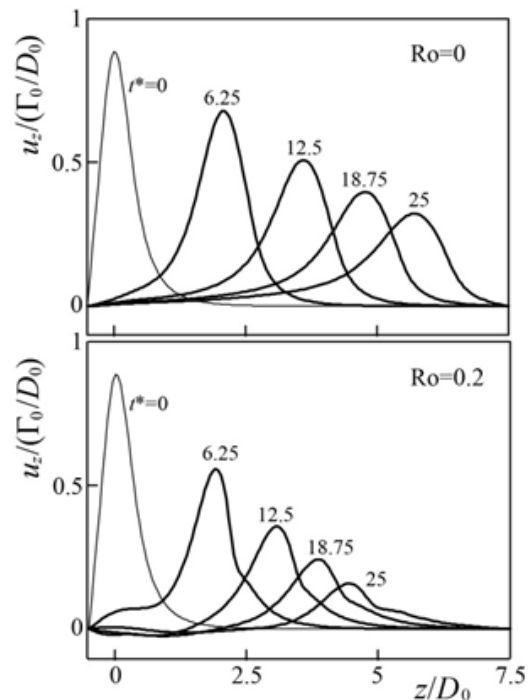


Figure 13: Distribution of axial velocity along centerline of vortex ring.

central axis, where the results at five time points for $\text{Ro}=0$ and 0.2 are plotted. When $\text{Ro}=0.2$, u_z lessens greatly, demonstrating the reduction of the strength for the vortex ring due to the field rotation. The position, where u_z takes its maximum value, corresponds to the center of the vortex core. When $\text{Ro}=0.2$, u_z decreases markedly at the head of the vortex core. This is because the secondary vortex ring with $\omega_\phi < 0$ and $u_z < 0$ exists there.

The time-evolution characteristics of the vortex ring are shown in Figure 14. The decrement of the circulation Γ becomes larger with the increase of Ro . The marked decrement occurs at $2.5 \leq t^* \leq 12.5$. This is

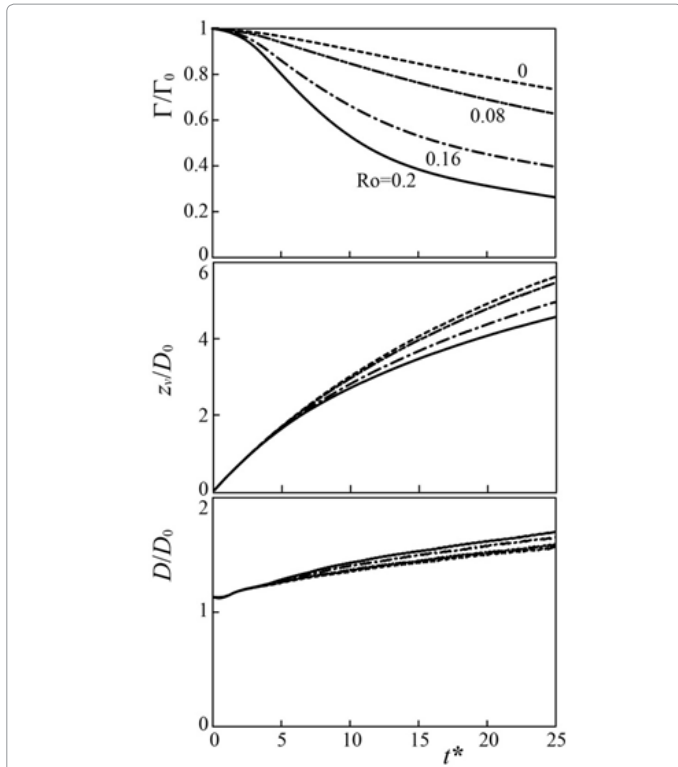


Figure 14: Effect of Ro on time-evolution characteristics of vortex ring.

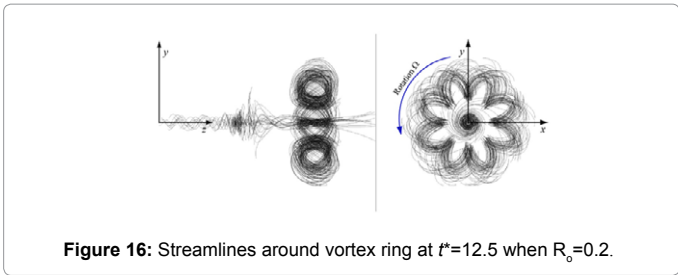


Figure 16: Streamlines around vortex ring at $t^*=12.5$ when $R_o=0.2$.

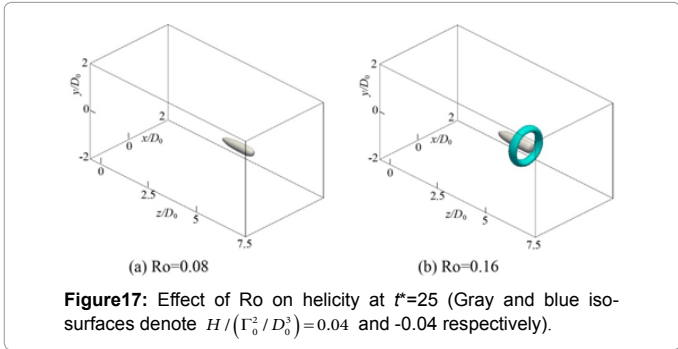


Figure 17: Effect of Ro on helicity at $t^*=25$ (Gray and blue iso-surfaces denote $H / (\Gamma_0^2 / D_0^3) = 0.04$ and -0.04 respectively).

because the velocity around the vortex ring is higher, and accordingly the Coriolis force affects more the vortex ring. The convection velocity of the vortex ring also lowers due to the reduction of Γ . The diameter D increases more with the increment of R_o . Because the secondary vortex ring with $\omega_\phi < 0$ appears at the head of the vortex ring as shown in Figure 11, and therefore it pushes the region with the positive azimuthal vorticity $\omega_\phi > 0$ in the radially outer direction.

Time evolution of helicity

The helicity $H (\mathbf{u} \cdot \boldsymbol{\omega})$ is zero on the non-rotating field. But it takes the finite values on the rotating field. Calculating the helicity H at $R_o=0.2$, it evolves with the passage of time as shown in Figure 15, where the iso-surfaces of $H / (\Gamma_0^2 / D_0^3) = \pm 0.04$ are plotted. The positive helicity appears around the central axis behind the vortex ring. This presents the streamwise longitudinal vortex composed of the positive axial vorticity ω_z induced by the Coriolis force and the positive axial velocity u_z in the wake of the vortex ring. The negative helicity distributes along the vortex core. This presents the swirling flow composed of the negative azimuthal velocity V_ϕ induced by the Coriolis force and the positive azimuthal vorticity ω_ϕ of the vortex ring.

Figure 16 shows the streamlines at $t^* = 12.5$ in the case of $R_o=0.2$. One can reconfirm the streamwise longitudinal vortex around the central axis behind the vortex core (the positive helicity) and the swirling flow along the vortex core (the negative helicity).

The iso-surfaces of the helicity $H / (\Gamma_0^2 / D_0^3) = \pm 0.04$ at $R_o=0.08$ and 0.16 are shown in Figure 17. The absolute value of the helicity decreases with the decrease of R_o , and the streamwise longitudinal vortex and swirling flow induced by the field rotation reduce their scales.

Conclusions

The behavior of a vortex ring on a field rotating with a constant angular velocity Ω is simulated. The vortex ring convects along the rotating axis of the field. The vortex in cell (VIC) method is employed for the simulation. The behavior at the rotation number $R_o (= 2\Omega D_0^2 / \Gamma_0)$

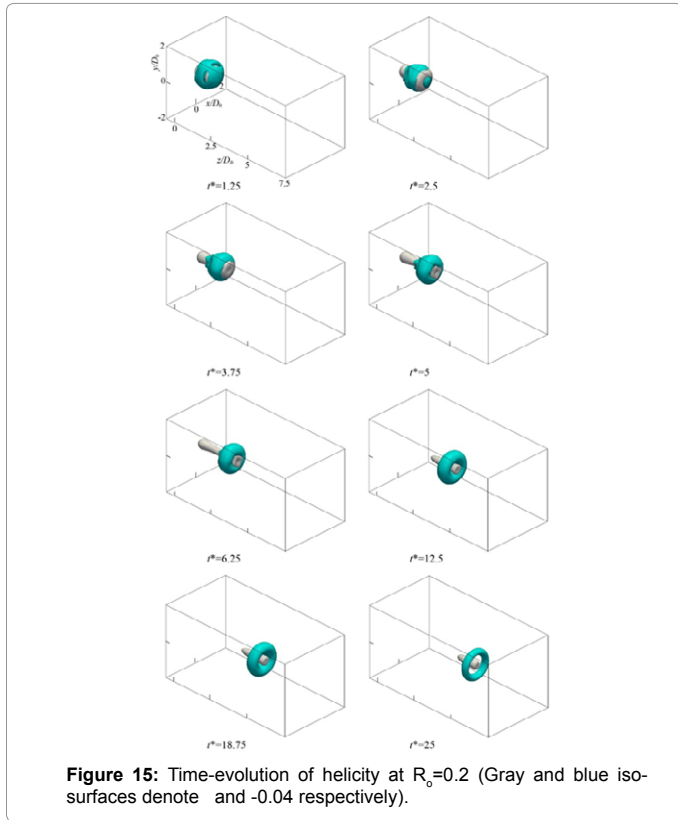


Figure 15: Time-evolution of helicity at $R_o=0.2$ (Gray and blue iso-surfaces denote $H / (\Gamma_0^2 / D_0^3) = \pm 0.04$ respectively).

of $0 \leq R_o \leq 0.4$ is simulated when the Reynolds number $R_c (= \Gamma_0 / \nu)$ is 500, where Γ_0 and D_0 are the circulation and diameter of the vortex ring at the initial time respectively. The results are summarized as follows:

(1) The vortex ring convects straight with maintaining its axisymmetric geometry in the same way on the non-rotating field. But the decrements of the vorticity and convection velocity with the passage of time become larger with the increment of R_o . This is because a secondary vortex ring, the vorticity of which is of opposite sign to the vortex ring, appears at the head of the vortex ring, and accordingly it interacts with the vortex ring.

(2) The circumferential flow with the velocity $u_\phi > 0$ toward the same direction as the rotating field occurs due to the Coriolis force around the central axis (rotating axis) behind the vortex ring. This demonstrates that the rotation yields the axial vorticity ω_z . The wake of the vortex ring and ω_z form the streamwise longitudinal vortex around the central axis.

(3) The circumferential flow with the azimuthal velocity $u_\phi < 0$ toward the opposite direction of the rotating field appears owing to the Coriolis force outside of the vortex core. The absolute value of the velocity is smaller than that of the flow around the central axis. The vorticity of the vortex ring and u_ϕ form the swirling flow along the vortex core.

(4) The secondary vortex rings occur at the head and in the rear of the vortex ring. The vorticity has the opposite sign to that of the vortex ring. The secondary vortex rings are induced by the fact that the Coriolis force acts on the circumferential flow with the velocity u_ϕ caused by the field rotation.

(5) The streamwise longitudinal vortex around the central axis and the swirling flow along the vortex core become larger with the increment of R_o . The increment in the diameter of the vortex ring with the passage of time is also larger. Because the secondary vortex rings appearing at the head of the vortex ring extrudes the vortex ring to the outside.

Nomenclatures

a : core radius of vortex ring

D : diameter of vortex ring

H : helicity = $\mathbf{u} \cdot \boldsymbol{\omega}$

\mathbf{k} : unit vector parallel to rotating axis

N_v : number of vortex elements

\mathbf{n} : unit normal vector

P : pressure

R_c : Reynolds number = Γ_0 / ν

R_o : rotation number = $2\Omega D_0^2 / \Gamma_0$

r : radius vector

S : distance from center of vortex core

t : time

t^* : non-dimensional time = $t / (D_0^2 / \Gamma_0)$

\mathbf{u} : velocity

W : redistribution function of vorticity

x, y, z : orthogonal coordinates

z_v : z -coordinate of center for vortex core

Γ : circulation

Δt : time increment

$\Delta x, \Delta y, \Delta z$: width of computational grid cell

ν : kinematic viscosity

ρ : density

ϕ : scalar potential

φ : angle between radius vector and x -axis

ψ : vector potential

Ω : angular velocity

$\boldsymbol{\omega}$: vorticity = $\nabla \times \mathbf{u}$

Subscripts

0 : initial value

x, y, z : components in directions of x, y and z

φ : azimuthal component (Table 1).

References

- Johnston JP, Halleen RM, Lezius DK (1972) Effects of spanwise rotation on the structure of two-dimensional fully developed turbulent channel flow. J Fluid Mech 56: 533-557.
- Kristoffersen R, Andersson HI (1993) Direct simulations of low-Reynolds-number turbulent flow in a rotating channel. J Fluid Mech 256: 163-197.
- Grundestam O, Wallin S, Johansson AV (2008) Direct numerical simulations of rotating turbulent channel flow. J Fluid Mech 598: 177-199.
- Charles G, Speziale (1982) Numerical study of viscous flow in rotating rectangular ducts. J Fluid Mech 122: 251-271.
- Kikuyama K, Murakami M (1983) Flows and pressure recovery in a rotating diffuser (Effects of inlet velocity distributions) Bull. JSME 26: 970-977.
- Rothe PH, Johnston JP (1976) Effects of system rotation on the performance of two-dimensional diffusers. J Fluid Eng 98: 422-429.
- Shariff K, Leonard A (1992) Vortex rings. Annu. Rev. Fluid Mech 24: 235-279.
- Eisenga AHM, Verzicco R, van Heijst GJF (1998) Dynamics of a vortex ring moving perpendicularly to the axis of a rotating fluid. J Fluid Mech 354: 69-100.
- Verzicco R, Orlandi P, Eisenga AHM, Van Heijst GJF, Carnevale GF (1996) Dynamics of a vortex ring in a rotating fluid. J Fluid Mech 317: 215-239.
- Brend MA, Thomas PJ (2009) Decay of vortex rings in a rotating fluid. J Physics of fluids 21:044105-1-044105-4.
- Cottet GH, Poncet P (2003) Advances in direct numerical simulations of 3D wall-bounded flows by Vortex-in-Cell methods. J Comput Phys 193: 136-158.
- Cocle R, Winckelmans G, Daeninck G (2008) Combining the vortex-in-cell and parallel fast multipole methods for efficient domain decomposition simulations. J Comput Phys 227: 9091-9120.
- Chatelain P, Curioni A, Bergdorf M, Rossinelli D, Andreoni W, et al. (2008) Billion vortex particle direct numerical simulations of aircraft wakes. Comput Methods Appl Mech Eng 197: 1296-1304.
- Uchiyama T, Yoshii Y, Hamada H (2013) Direct numerical simulation of a turbulent channel flow by an improved vortex in cell method. Int J Numerical Methods for Heat and Fluid Flow 24: 103-123.
- Cottet G H, Koumoutsakos P (2000) Vortex Methods: Theory and Applications. Cambridge Univ. Press, Cambridge.

16. Uchiyama T, Kobayashi M, Iio S, Ikeda T (2013) Direct numerical simulation of a jet issuing from rectangular nozzle by the vortex in cell method. *Open J Fluid Dynamics* 3: 321-330.
17. Stanaway SK, Cantwell BJ, Spalart PR (1988) A numerical study of viscous vortex rings using a spectral method. NASA TM-101041.
18. Wee D, Ghoniem AF (2006) Modified interpolation kernels for treating diffusion and remeshing in vortex methods. *J Comput Phys* 213: 239-263.